

Sub-diurnal asymmetric warming has amplified atmospheric dryness since the 1980s

Received: 16 January 2025

Accepted: 26 August 2025

Published online: 09 September 2025

 Check for updatesZiqian Zhong¹, Hans W. Chen¹✉, Aiguo Dai², Tianjun Zhou³, Bin He⁴ & Bo Su^{4,5,6}

Rising atmospheric vapor pressure deficit (VPD)—a measure of atmospheric dryness, defined as the difference between saturated vapor pressure (SVP) and actual vapor pressure (AVP)—has been linked to increasing daily mean near-surface air temperatures since the 1980s. However, it remains unclear whether the faster increases in daily maximum temperature (T_{\max}) relative to daily minimum temperature (T_{\min}) have contributed to rising VPD. Here, we show that the faster rise in T_{\max} compared with T_{\min} over land has intensified VPD from 1980 to 2023. This sub-diurnal asymmetric warming has driven a larger SVP increase than would occur under uniform temperature rise, while AVP is more strongly influenced by T_{\min} . Using reanalysis data, we estimate that asymmetric warming has contributed an additional ~18% to the increase in global land VPD. Sub-daily station observations corroborate this pattern, with asymmetric warming accounting for ~30% of VPD intensification across all stations. Our findings indicate that sub-diurnal asymmetric warming has substantially amplified global warming's effect on atmospheric dryness over the past four decades, with significant implications for terrestrial water availability and carbon cycling.

Global surface temperatures have been rising, with warming accelerating across nearly all continents in recent decades^{1,2}. The past nine years, from 2015 to 2023, have been the warmest on record^{3–5}. Rising air temperatures increase the near surface (~2 m) saturation vapor pressure (SVP)—the atmosphere's capacity to hold water vapor—by roughly 7% per 1°C warming according to the Clausius-Clapeyron relationship^{6,7}. As the near surface actual vapor pressure (AVP) has generally increased at a lower rate than SVP, their difference, known as the atmospheric vapor pressure deficit (VPD), has increased in all climatic zones since 1980s^{8–10}. The notable VPD increase in recent decades has significantly affected vegetation growth and productivity^{11–14},

maize yield^{15,16}, land evapotranspiration^{17,18}, and the occurrence of wildfires^{19,20} worldwide.

VPD changes are controlled by both atmospheric temperature and moisture variations. This is because SVP is almost exclusively determined by air temperature, while AVP depends on both temperature and moisture variations. Another common metric for the water vapor content in the atmosphere is relative humidity (RH), defined as the ratio of AVP to SVP. Unlike the increase in SVP due to rising air temperatures, the long-term trend of globally averaged near-surface RH over land has remained small until the early 2000s²¹, and a significant decline has been reported after the year 2000^{22,23}. The

¹Department of Space, Earth and Environment, Division of Geoscience and Remote Sensing, Chalmers University of Technology, SE-412 96

Gothenburg, Sweden. ²Department of Atmospheric and Environmental Sciences, University at Albany, State University of New York, Albany, NY 12222, USA.

³State Key Laboratory of Numerical Modeling for Atmospheric Sciences and Geophysical Fluid Dynamics, Institute of Atmospheric Physics, Chinese Academy of Sciences, Beijing 100029, China. ⁴State Key Laboratory of Earth Surface Processes and Resource Ecology, Faculty of Geographical Science, Beijing Normal University, Beijing 100875, China. ⁵Regional Climate Group, Department of Earth Sciences, University of Gothenburg, S-40530 Gothenburg, Sweden.

⁶Stockholm Resilience Centre, Stockholm University, 10691 Stockholm, Sweden. ✉e-mail: hans.chen@chalmers.se

factors contributing to the spatial patterns of RH trends on a global scale remain unclear²⁴. Additionally, although surface air temperature influences both SVP and RH, and is a key climatic factor affecting VPD, the impact of sub-daily temperature variations on VPD is often overlooked, even though diurnal temperature variations have been found to be the main driver of RH diurnal variations²¹.

Given the approximately exponential relationship between air temperature and SVP²⁵, a temperature increase during warmer daytime hours results in a larger SVP increase than an equivalent warming during cooler nights. Recent studies have found that daily maximum temperatures (T_{\max}) have increased more rapidly than daily minimum temperatures (T_{\min}) over land since the 1980s^{26,27}. This sub-diurnal asymmetric warming is primarily driven by changes in solar radiation, which is closely linked to variations in cloud cover and aerosol emissions^{26,28,29}. The resulting increase in the diurnal temperature range ($DTR = T_{\max} - T_{\min}$) marks a shift from previously faster nighttime warming to faster daytime warming^{30–33}. This shift raises the question: What is the relative importance of T_{\max} and T_{\min} in driving VPD variations?

To answer this question, we employed ridge regression³⁴ to assess the effects of interannual variations in T_{\max} and T_{\min} on VPD. Considering the potential complex interactions and non-linear relationships among the environmental factors examined, we further applied a Random Forest (RF) regression model³⁵ enhanced with Shapley Additive Explanations³⁶ (RF-SHAP) as a complementary approach. The RF approach delivers robust predictive performance by effectively capturing intricate, non-linear data patterns that traditional linear models may not adequately capture. In addition, the SHAP framework provides a clearer understanding of each environmental factor's relative contribution. Finally, using flux tower observations, we examined daily temperature–VPD relationships for both T_{\max} and T_{\min} , then implemented RF regression to evaluate the role of sub-diurnal asymmetric warming in driving long-term VPD changes.

Results

Interannual analysis

In our study, we used both sub-daily in-situ observations from the HadISD dataset³⁷ and hourly data from the ERA5-Land reanalysis³⁸. Previous research has shown that the ERA5 reanalysis effectively captures diurnal variations in climatic variables^{39,40}. However, in some regions—such as East Asia—correlations between DTR values derived from the ERA5-Land reanalysis and co-located HadISD observations are notably weaker (see Supplementary Discussion 1, Supplementary Fig. 1). Therefore, most of our analyses were conducted using both the HadISD and ERA5-Land datasets in parallel, to provide complementary insights and mutual support.

We first identified the annual trends in DTR and VPD over the period 1980–2023. VPD can be calculated using the following equation⁴¹:

$$VPD = SVP \times (1 - RH) \quad (1)$$

The significant ($p < 0.05$) increase in annual-mean VPD (Supplementary Fig. 2a), at an average rate of 0.24 hPa per decade across 1398 stations, can thus be attributed to a substantial rise in SVP and a significant decrease in RH (Supplementary Fig. 2c). Previous regional studies have suggested that RH measurements may exhibit discontinuities due to recent hygrometer changes⁴². However, these discontinuities are localized and limited in number, and the associated uncertainties are essentially negligible when assessing large-scale characteristics of RH⁴³. The positive VPD trends were most pronounced in the mid- to low-latitude regions based on the ERA5-Land reanalysis dataset (Supplementary Fig. 3f).

Due to the faster increase in T_{\max} than in T_{\min} , the mean DTR across all stations has significantly increased at an average rate of

0.10 °C per decade. Spatially, based on the ERA5-Land dataset, we found that 58% of global land areas experienced an increase in DTR. Notably, the area with a significant increase in DTR (30%) was nearly twice as large as the area with a significant decrease (15%) during 1980–2023 (Fig. 1a). This finding is consistent with previous studies reporting increasing DTR in recent decades^{26,27}. Regions showing DTR increases were mainly located in western North America, South America, Europe, central Africa, Central Asia, eastern China, and Australia. We found a strong correlation between the annual average DTR and VPD during 1980–2023 (correlation coefficient $r = 0.88$, $p < 0.05$) across all stations (Supplementary Fig. 2a). This correlation remained strong and significant ($r = 0.64$, $p < 0.05$) after removing their long-term linear trends. The ERA5-Land reanalysis dataset also showed similar increasing trends in annual mean DTR and VPD over land (Supplementary Fig. 2d), along with a significant correlation between them ($r = 0.76$, $p < 0.05$ for the raw time series and $r = 0.60$, $p < 0.05$ after detrending).

We then investigated the impact of interannual variations in DTR on VPD. Specifically, we employed ridge regression³⁴ and an RF regression model, using DTR, daily mean temperature (T_{mean}), and soil moisture (SM) as independent variables, and VPD as the dependent variable (Supplementary Fig. 4):

$$VPD \sim f(DTR, T_{\text{mean}}, SM) \quad (2)$$

where f represents the functional relationship between VPD and the independent variables. In addition to this formulation, VPD was also modeled as a function of T_{\max} , T_{\min} , and SM:

$$VPD \sim f(T_{\max}, T_{\min}, SM) \quad (3)$$

SM was included as an independent variable in both equations because it is a key source of surface vapor and physically influences VPD through its role in evaporation. Moreover, SM can modulate DTR by enhancing evaporative cooling, which typically has a stronger effect on T_{\max} than T_{\min} ⁴⁴. Therefore, it is essential to account for the influence of SM when assessing the DTR–VPD relationship in the regression models. Based on the ridge regression model defined in Eq. (2) and detrended, standardized interannual variables, we found that interannual fluctuations in VPD were positively associated with DTR variations across both station-based observations and ERA5-Land grid points during 1980–2023 (Fig. 1b). We further applied the ridge regression model defined in Eq. (3) to assess the differential impacts of sub-daily temperatures on VPD (Supplementary Fig. 5). Overall, T_{\max} exhibited a strong positive influence on interannual VPD variability (Fig. 1c), whereas T_{\min} showed a relatively weaker effect across both station-based observations and ERA5-Land grid points (Fig. 1e). We further estimated the relative importance of T_{\max} and T_{\min} in driving interannual VPD variability using the RF-SHAP framework (Supplementary Fig. 6). This approach mitigates issues of multicollinearity and captures nonlinear interactions. Relative importance was calculated as the normalized magnitude of the absolute SHAP values, which represent the importance of each predictor in the RF regression model. The relative importance of T_{\max} accounted for a median of 41% of VPD variability across all stations (Fig. 1d) and 40% across all ERA5-Land grid points (Fig. 1f), whereas the relative importance of T_{\min} was notably lower, with a median of 18% across all stations (Fig. 1d) and 22% in ERA5-Land (Fig. 1f). These results indicate an asymmetric effect of T_{\max} and T_{\min} on atmospheric dryness, with T_{\max} playing a more dominant role than T_{\min} in driving the interannual variability of VPD.

VPD can be expressed as either $VPD = SVP - AVP$ or $VPD = SVP \times (1 - RH)$ (Eq. 1), indicating that VPD variations depend on changes in SVP and either AVP or RH. Using detrended interannual daily mean variables, we conducted further analyses based on three regression

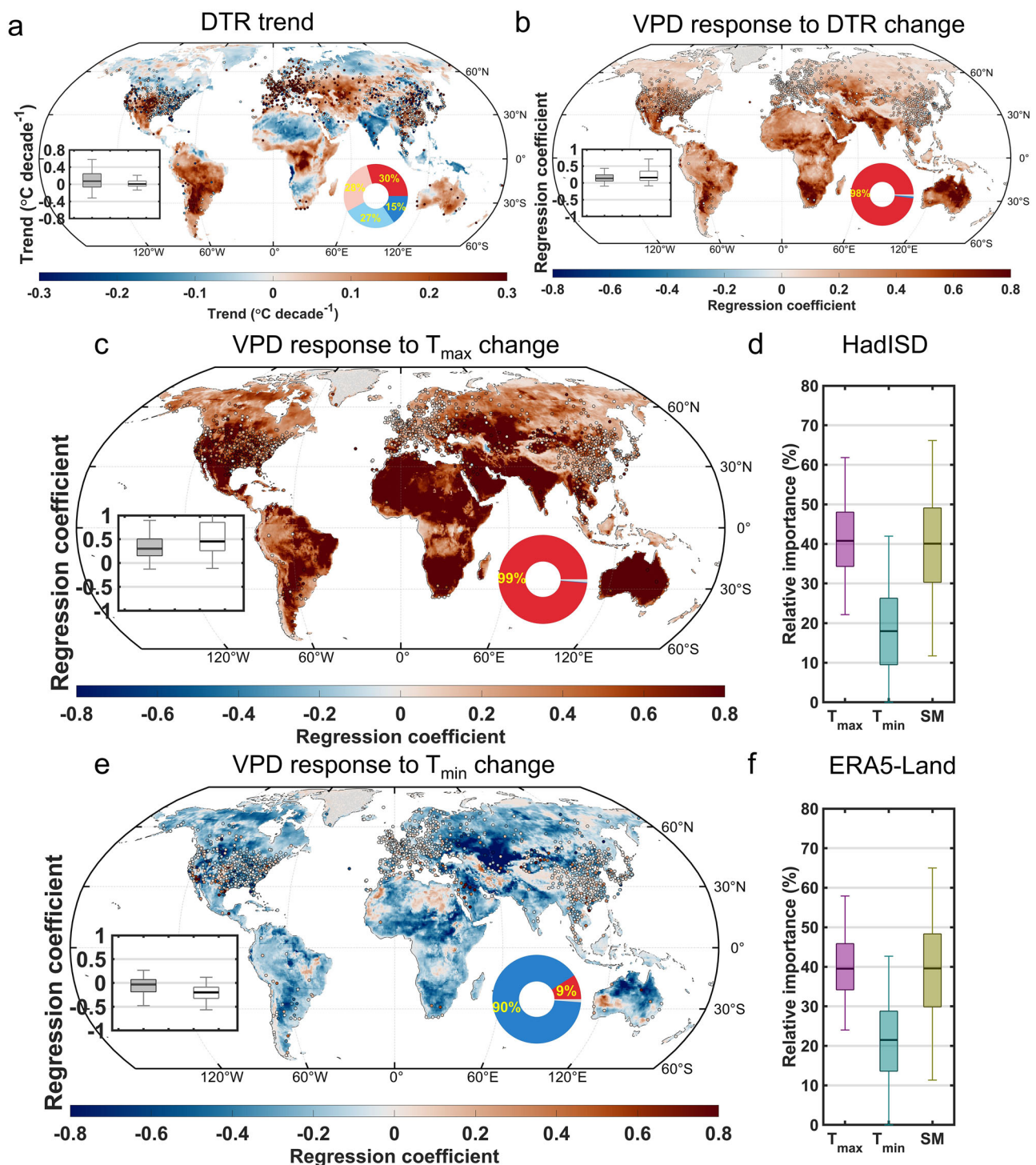


Fig. 1 | Relative importance of daily maximum (T_{\max}) and minimum temperatures (T_{\min}) in interannual vapor pressure deficit (VPD) variations from 1980 to 2023. **a Spatial distribution of the trend in diurnal temperature range (DTR) over land areas. Inset shows boxplots of trends across observation stations (solid boxes) and ERA5-Land grid points (hollow boxes). Pie chart shows the percentage of land area with significantly ($p < 0.05$) positive (red), weak positive (light red), weak negative (light blue), and significantly negative (blue) trends, based on ERA5-Land data. **b** Spatial distribution of ridge regression (RR) coefficients of interannual VPD with respect to DTR, derived from the RR model defined in Eq. (2). **c, e** Spatial distribution of RR coefficients of interannual VPD with respect to T_{\max} (c) and T_{\min} (e), derived from the RR model defined in Eq. (3). Insets in **b, c, and e** show boxplots of RR coefficients across observation stations (solid boxes) and grid points (hollow**

boxes). Pie charts show the percentage of land area with positive (red), negative (blue), and non-significant (light grey) RR coefficients based on ERA5-Land data. “Non-significant” refers to cases where none of the coefficients in the RR model are statistically significant. Stations (1.07% in **b**; 1.29% in **c, e**) and areas (1.10% in **b**; 1.11% in **c, e**) with non-significant RR coefficients are masked in light grey and excluded from RR model-based analysis. **d, f** Relative importance of interannual T_{\max} , T_{\min} , and soil moisture (SM) in driving interannual VPD variability based on the Random Forest regression model defined in Eq. (3), evaluated across stations (**d**) and ERA5-Land grid points (**f**). All variables in the regressions are detrended and standardized annual averages. In all boxplots, the height of each box represents the interquartile, with the thick black line indicating the median, and the edges denoting the first and third quartiles. Whiskers extend to the 2.5th and 97.5th percentiles.

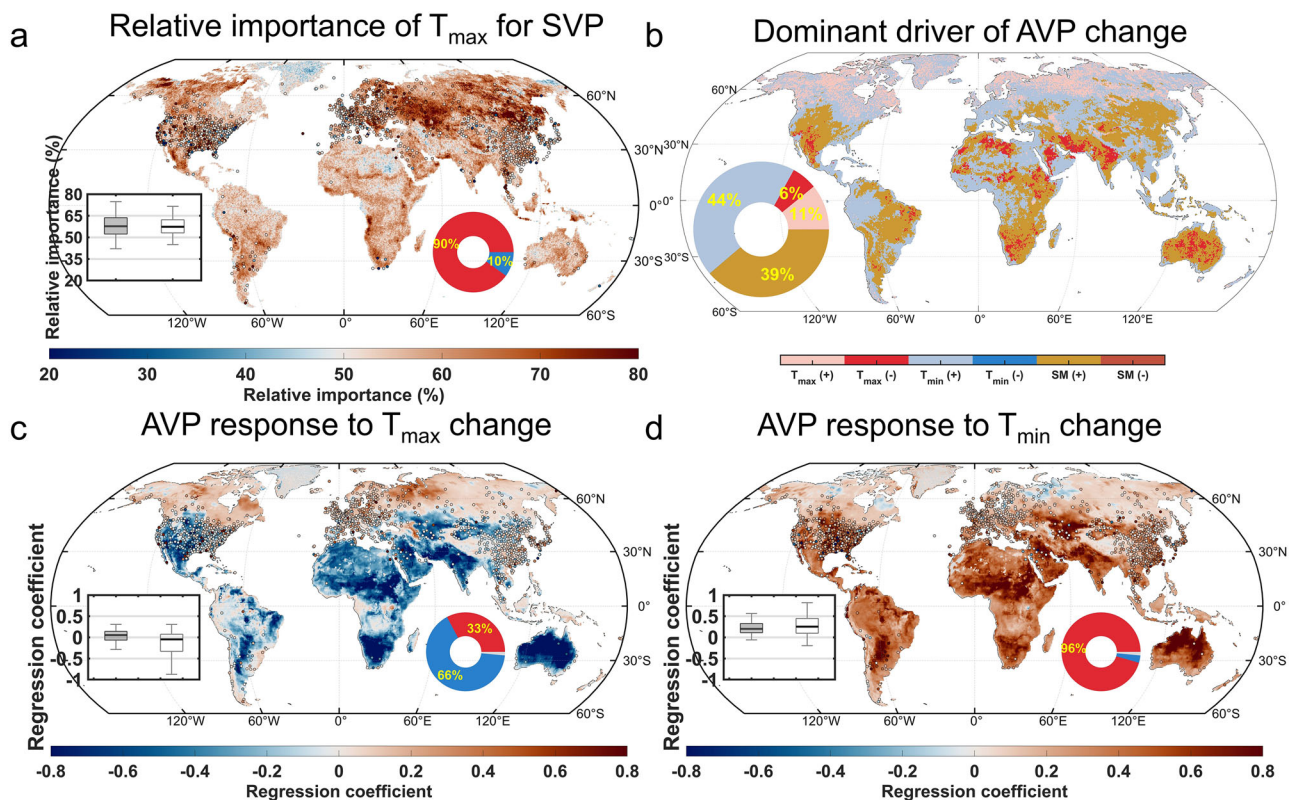


Fig. 2 | Relative importance of daily maximum (T_{\max}) and minimum temperatures (T_{\min}) in interannual variations of saturation vapor pressure (SVP) and actual vapor pressure (AVP) from 1980 to 2023. **a Spatial distribution of relative importance of T_{\max} in interannual SVP, identified using the Random Forest (RF) regression model defined in Eq. (4) with the Shapley Additive Explanations (SHAP) framework. Inset shows boxplots of relative importance (%) across stations (solid boxes) and ERA5-Land grid points (hollow boxes). Pie chart shows the percentage of land area where T_{\max} importance exceeds 50% (red) or is below 50% (blue), based on ERA5-Land data. **b** Spatial distribution of the dominant driver of interannual AVP changes, identified using the RF regression model defined in Eq. (5) with the SHAP framework, based on ERA5-Land data. Pie chart shows the percentage of land area where AVP is dominantly driven by T_{\max} , T_{\min} , or soil moisture (SM), with either a positive (+) or negative (−) influence. **c** and **d** spatial distribution of ridge regression**

(RR) coefficients of interannual AVP with respect to T_{\max} (**c**) and T_{\min} (**d**), derived from the RR model defined in Eq. (5). Insets show boxplots of RR coefficients across observation stations (solid boxes) and grid points (hollow boxes). Pie charts show the percentage of land area with positive (red), negative (blue), and non-significant (light grey) RR coefficients based on ERA5-Land data. “Non-significant” refers to cases where none of the coefficients in the RR model are statistically significant. Stations (4.36%) and areas (1.45%) with non-significant RR coefficients are masked in light grey and excluded from the analysis. All variables in the regressions are detrended and standardized annual averages. In all boxplots, the height of each box represents the interquartile, with the thick black line indicating the median, and the edges denoting the first and third quartiles. Whiskers extend to the 2.5th and 97.5th percentiles.

models:

$$\text{SVP} \sim f(T_{\max}, T_{\min}) \quad (4)$$

$$\text{AVP} \sim f(T_{\max}, T_{\min}, \text{SM}) \quad (5)$$

$$\text{RH} \sim f(T_{\max}, T_{\min}, \text{SM}) \quad (6)$$

Based on the RF regression model defined in Eq. (4) and the RF-SHAP framework (Supplementary Fig. 7), we found that the interannual variations in SVP were primarily determined by T_{\max} , with T_{\max} exerting a greater impact on SVP than T_{\min} across nearly 90% of land areas in the ERA5-Land dataset (Fig. 2a). The stronger influence of T_{\max} on SVP is due to the near-exponential relationship between temperature and SVP, meaning the rate of SVP increase is greater at higher temperatures. For instance, according to the Clausius-Clapeyron relationship, while a 1 °C increase at global average land T_{\min} (8.6 °C) leads to a 0.78 hPa rise in SVP, the same temperature increase at global average land T_{\max} (18.2 °C) results in a 1.35 hPa rise—roughly 72% higher (Supplementary Fig. 8a). This differential effect is even more pronounced in low-to-mid-latitudes, where a 1 °C increase at

typical land T_{\max} (25.5 °C) produces a 76% higher SVP compared to T_{\min} (15.8 °C). This illustrates why T_{\max} exerts a stronger influence on SVP than T_{\min} , and indicates that in warmer conditions, the difference in the impact of T_{\max} and T_{\min} on SVP will become even more pronounced.

Based on the ridge regression model defined in Eq. (5), we found that T_{\min} has significantly affected AVP across 93% of the land area based on the ERA5-Land dataset (Supplementary Fig. 9d). Overall, T_{\min} has exerted a positive influence on AVP, with 96% of land area exhibiting positive regression coefficients based on the ERA5-Land dataset (Fig. 2d). Using the RF-SHAP framework with the same independent and dependent variables (Supplementary Fig. 10), we found that T_{\min} was the dominant driver of AVP over 44% of land areas, primarily located in the mid-latitudes, where it has exerted a positive influence (Fig. 2b). Here, the “dominant driver” refers to the variable that contributes most to the RF regression model output, as indicated by the highest mean absolute SHAP value among all predictors. The direction of influence—positive or negative—is determined by the Theil–Sen slope between the variable’s values and their corresponding SHAP values. In contrast, T_{\max} was the dominant driver with a positive influence over only 11% of land areas, and with a negative influence over 6%. This widespread positive influence of T_{\min} on AVP may also

have contributed to its broad positive effect on RH. According to ridge regression results from Eq. (6), 95% of grid cells had positive regression coefficients for the effect of T_{\min} on RH based on the ERA5-Land dataset (Supplementary Fig. 11d). The positive effect of T_{\min} on AVP (Fig. 2d) can be supported by the general alignment of dew point temperature with T_{\min} ⁴⁵, along with the near-exponential relationship between AVP and dew point temperature according to the Clausius-Clapeyron relationship. Air temperature governs the maximum amount of water vapor that the atmosphere can hold. Typically, over land—especially under more humid conditions—RH often approaches 100% around the time of T_{\min} , while AVP (or specific humidity) is relatively stable through the 24-hr diurnal cycle²¹. This suggests that T_{\min} largely controls the water vapor content or AVP in the air when it is close to saturation. Although slight diurnal fluctuations in water vapor content may occur, T_{\min} plays a more substantial role than T_{\max} in controlling the daily-mean water vapor content (Supplementary Fig. 8b).

We found that the positive response of AVP to T_{\max} was relatively heterogeneous and regionally variable compared to its response to T_{\min} (Fig. 2b, c). During the daytime, increased temperature typically elevates VPD, which enhances land evapotranspiration over wet surfaces⁴⁶, thereby increasing atmospheric water vapor. However, over drylands, the relationship between temperature/VPD and evapotranspiration becomes more complex, particularly when considering plant physiological processes⁴⁷. Using half-hourly observational data from FLUXNET tower sites⁴⁸ (Supplementary Fig. 12), we found that the diurnal cycle of VPD closely mirrors that of temperature ($R^2 = 0.985 \pm 0.014$; mean \pm one standard deviation across all sites). This similarity arises because SVP, which is strongly temperature-dependent ($R^2 = 0.997 \pm 0.002$), exhibits greater diurnal variation than AVP, with daily standard deviations of 2.76 hPa versus 0.17 hPa, respectively (Supplementary Fig. 13). Consequently, higher T_{\max} produces greater daily maximum VPD. During high VPD conditions, plant stomata tend to partially close in response to increased atmospheric dryness^{49,50}. This “feed-forward” response⁵¹ reduces transpiration rates under high VPD conditions²⁵, thereby limiting increases in AVP. The inhibitory effect is particularly pronounced in water-limited areas of low- to mid-latitudes (Fig. 2c), where the climate is relatively hot and dry.

Daily analysis

The above findings suggest that changes in T_{\max} and T_{\min} have different impacts on daily-mean VPD. When T_{\max} increases, it will lead to a larger increase in SVP than AVP and result in a noticeable increase in VPD. In contrast, for an equivalent increase in T_{\min} , the resulting increase in SVP is smaller, while RH will increase in most regions, thus partially offsetting the increase in VPD associated with rising T_{\max} . Building on observational data from FLUXNET tower sites, we further investigated the impact of diurnal temperatures on VPD after accounting for the influence of SM on the relationship between DTR and VPD. We conducted this analysis because increased SM can enhance evaporative cooling, which reduces T_{\max} and consequently lowers DTR⁴⁴. Simultaneously, the increased SM raises AVP and RH, further decreasing VPD^{52,53}. These processes could lead to a positive correlation between DTR and VPD.

To mitigate the influence of SM, we segmented the daily data into different bins based on the percentiles of the surface soil water content (SWC) within each flux tower site. Before the analysis, we employed Fourier transform-based filtering⁵⁴ (Supplementary Fig. 14) to remove seasonal variations from the daily variables. In all bins, the correlation between SWC and either VPD or DTR was generally weak, indicating decoupling^{50,55} between SWC and VPD or DTR within each bin (Supplementary Fig. 15a). We then compared the partial correlations between SVP, AVP, and RH with T_{\max} or T_{\min} within each bin (Fig. 3). In the partial correlation analysis, we accounted for the influence of T_{\min}

when estimating the correlations between T_{\max} and SVP, AVP, or RH. Similarly, we controlled for T_{\max} when calculating correlations with T_{\min} . Across all bins, T_{\max} showed a stronger correlation with SVP than T_{\min} , while T_{\min} exhibited a stronger positive correlation with AVP than T_{\max} . Since RH is the ratio between AVP and SVP, T_{\max} was generally negatively correlated with RH, while T_{\min} showed a positive correlation with RH. These findings, when considered alongside Eq. (1), indicate a strong positive correlation between VPD and T_{\max} , and a weak positive or even negative correlation between VPD and T_{\min} . This is consistent with the results of the partial correlation analysis between VPD and T_{\max} or T_{\min} (Supplementary Fig. 15b). These results further demonstrate the asymmetric effect of T_{\max} and T_{\min} on VPD, even after accounting for soil moisture effects.

Trend analysis

The preceding analysis reveals asymmetric effects of T_{\max} and T_{\min} on VPD at both interannual and daily scales. To further quantify the long-term impact of sub-diurnal asymmetric warming on VPD changes, we employed monthly, non-detrended variables—including DTR, T_{mean} , and SM—in an RF regression model as defined in Eq. (2) to predict monthly VPD values from 1980 to 2023. This RF approach was specifically chosen to capture the complex nonlinear relationships among these variables. We first trained the model to optimize its parameters, and then applied the trained model on the input data to obtain fitted VPD values ($\text{VPD}_{\text{fitted}}$). The median out-of-bag R^2 for the RF models reached 0.91 for the HadISD dataset and 0.96 for the ERA5-Land dataset (Supplementary Fig. 16a), indicating that the models effectively capture most of the variance in VPD over land. Subsequently, three sensitivity experiments (see Methods) were conducted, one for each independent variable, keeping the tested variable constant at its mean value for each month during the control period (the initial three years, 1980–1982), while the other two variables varied according to the input. The difference between $\text{VPD}_{\text{fitted}}$ and the estimated VPD from each sensitivity experiment was considered the contribution of DTR, T_{mean} , and SM change to the VPD change, denoted as VPD_{DTR} , $\text{VPD}_{T_{\text{mean}}}$, and VPD_{SM} , respectively.

On average, across all stations from 1980 to 2023, VPD_{DTR} increased at a rate of 0.06 hPa per decade ($p < 0.05$, Fig. 4a). An upward trend in VPD_{DTR} was observed at 80% of the stations, with 45% showing a statistically significant increase ($p < 0.05$, Fig. 4d). We then focused on the contribution rate of DTR change to the VPD increase, defined as the ratio of the slopes of VPD_{DTR} and $\text{VPD}_{\text{fitted}}$. On average, this contribution rate reached approximately 30% across all stations (Fig. 4a). Using the ERA5-Land dataset, DTR changes contributed an average of 18% to the VPD increase across land areas (Supplementary Fig. 17a). For the spatial analysis, we concentrated on stations where $\text{VPD}_{\text{fitted}}$ exhibited a significant increase ($p < 0.05$), representing about 66% of all stations. Here, the median contribution rate of DTR change to VPD increase reached 35% (Supplementary Fig. 18). According to ERA5-Land, the median contribution rate reached 22% in regions where VPD showed a significant increase. These results indicate that the increase in DTR has played a notable role in promoting the rise in VPD since the 1980s.

To further investigate the potentially distinct long-term impacts of T_{\max} and T_{\min} increases on VPD, we quantified the contributions of changes in monthly variables to SVP (Supplementary Fig. 19) and RH (Supplementary Fig. 20) changes using RF models as defined in Eqs. (4) and (6), respectively. On average, the contribution of T_{\max} to SVP ($\text{SVP}_{T_{\max}}$) was greater than that of T_{\min} ($\text{SVP}_{T_{\min}}$). The growth rate of $\text{SVP}_{T_{\max}}$ exceeded that of $\text{SVP}_{T_{\min}}$ in most mid-latitude regions, including southwestern North America, central and eastern South America, southern Europe, central Africa, Central Asia, and Australia (Fig. 4e). The contribution of T_{\max} to RH showed a significant decreasing trend (-0.33% per decade, $p < 0.05$, based on observations, Fig. 4c; and -0.34% per decade, $p < 0.05$, over land in the ERA5-Land

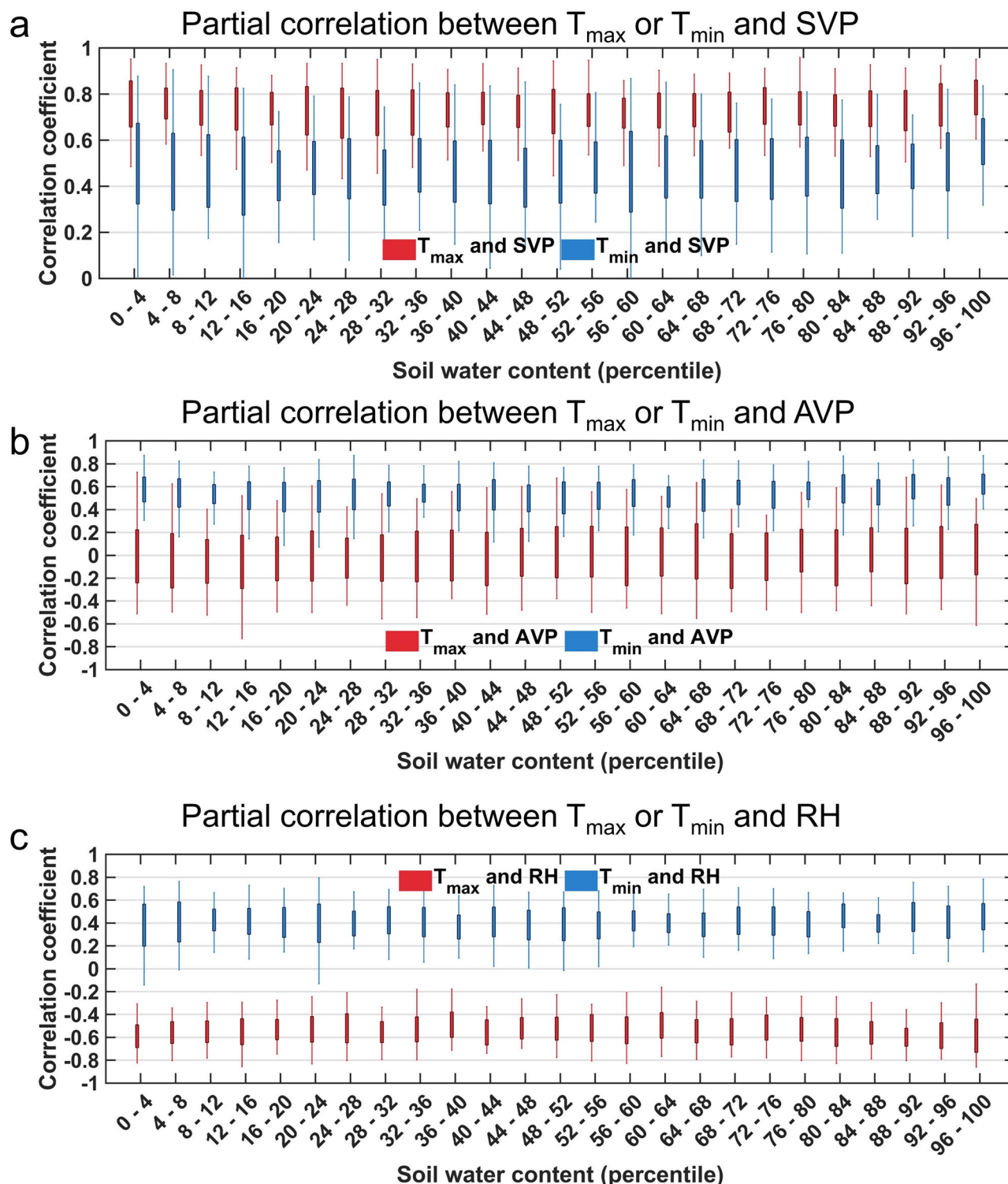


Fig. 3 | Asymmetric effects of daily maximum (T_{\max}) and minimum temperatures (T_{\min}) on saturated vapor pressure (SVP), actual vapor pressure (AVP), and relative humidity (RH). Assessment of the partial correlation between T_{\max} or T_{\min} and SVP (a), AVP (b), and RH (c) while controlling for the other variable across

different soil water content percentiles at all FLUXNET sites. The height of each box represents the interquartile range of correlation coefficients across different stations, with the edges denoting the first and third quartiles. Whiskers extend to the 2.5th and 97.5th percentiles of the correlation coefficient.

reanalysis, Supplementary Fig. 17c), which was widespread across most of the land areas except for northern North America and India. In contrast, the contribution of T_{\min} to RH exhibited a slight but significant increasing trend (0.13% per decade, $p < 0.05$, across stations; and 0.13% per decade, $p < 0.05$, over land in the ERA5-Land dataset), which was prevalent across most land areas except for the western

United States and Central Asia (Fig. 4g). This analysis reinforces that over the past few decades, changes in T_{\max} and T_{\min} have had different effects on both SVP and RH. Generally, increases in T_{\max} have had a bigger impact on increasing SVP than T_{\min} . Additionally, while increases in T_{\min} generally appear to have a positive effect on RH, increases in T_{\max} could contribute to decreased near-surface RH over

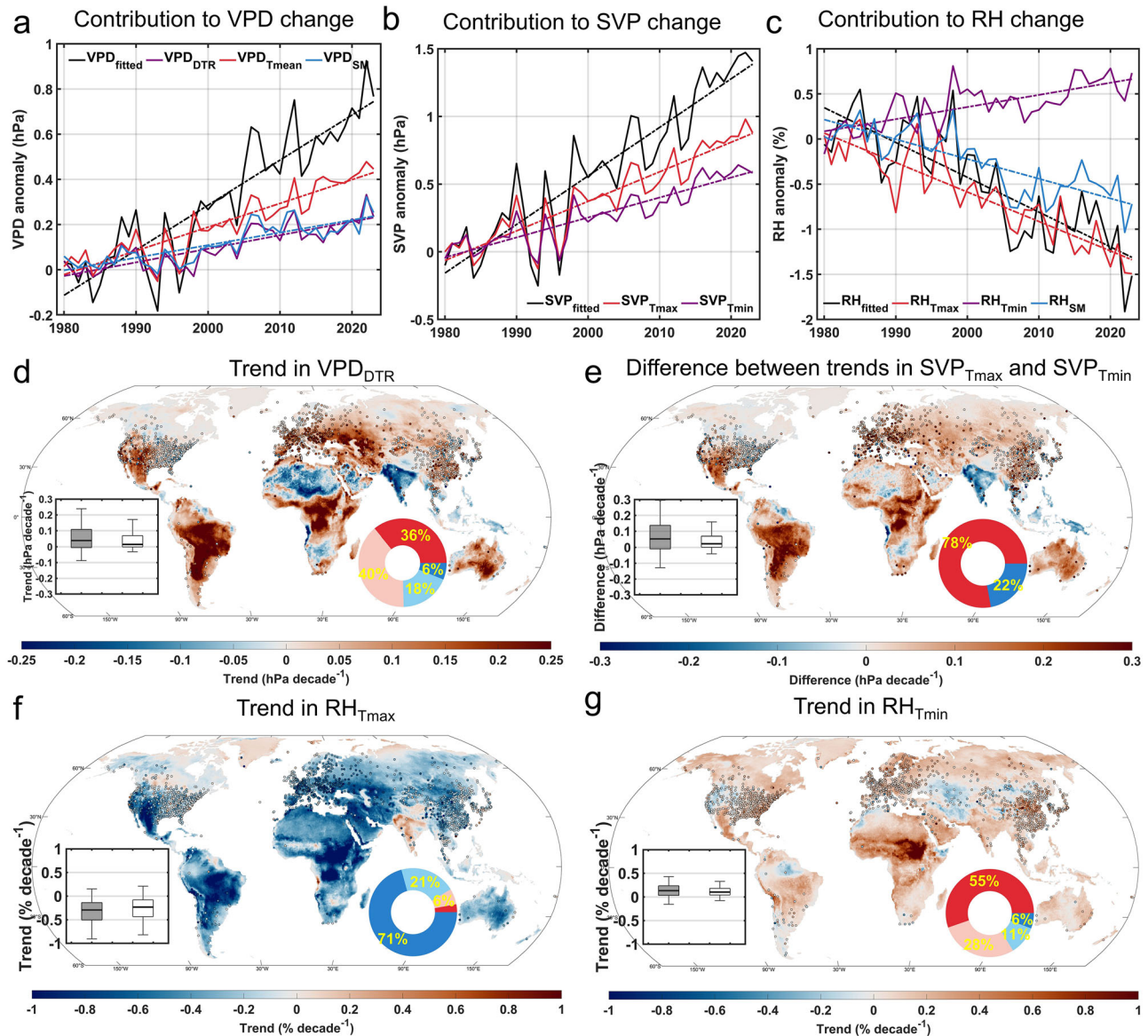


Fig. 4 | Contribution of sub-diurnal asymmetric warming to trends in saturated vapor pressure (SVP), relative humidity (RH), and vapor pressure deficit (VPD) from 1980 to 2023. a–c Variations and changes in the annual average model-fitted (subscript fitted) VPD (a), SVP (b), and RH (c), and the contributions of diurnal temperature range (subscript DTR), daily mean temperature (subscript T_{mean}), soil moisture (subscript SM), daily maximum temperature (subscript T_{max}) and daily minimum temperature (subscript T_{min}) to the variations and changes over land. The model-fitted values are anomalies calculated by subtracting the mean values for the control period (1980–1982). The dashed lines show the linear trends obtained from linear regressions. **d, f** and **g** Spatial distribution of trends in VPD_{DTR} (d), RH_{Tmax} (f), and RH_{Tmin} (g). Insets show boxplots of trends across observation

stations (solid boxes) and ERA5-Land grid points (hollow boxes). Pie charts show the percentage of land area with significantly ($p < 0.05$) positive (red), weak positive (light red), weak negative (light blue), and significantly negative (blue) trends, based on ERA5-Land data. **e**, Spatial distribution of differences between trends in SVP_{Tmax} and SVP_{Tmin}. Insets show boxplots of differences across observation stations (solid boxes) and ERA5-Land grid points (hollow boxes). Pie chart shows the percentage of land area with positive (red) and negative (blue) differences based on ERA5-Land data. In all boxplots, the height of each box represents the interquartile range of trends or differences across different stations or grid points, with the thick black line indicating the median, and the edges denoting the first and third quartiles. Whiskers extend to the 2.5th and 97.5th percentiles.

many land regions (Supplementary Fig. 11c). Due to these dual effects, the asymmetric warming characterized by daytime warming and increasing DTR over the past forty years has exacerbated atmospheric dryness over most land areas.

These results raise important questions that warrant further exploration: did VPD decline prior to 1980, and if so, was it related to faster nighttime warming observed during that period? To investigate this question, we extended the study period back to 1950 using the ERA5-Land dataset. We found that, over land, VPD significantly declined from the 1950s to the mid-1970s at a rate of -0.25 hPa per decade ($p < 0.05$), reaching a minimum around 1976 (Supplementary

Fig. 21). This decline was primarily associated with a significant decrease in T_{max} (-0.13 °C per decade, $p < 0.05$), while T_{min} showed little change (-0.03 °C per decade, $p > 0.05$) during 1950–1976. In contrast, during the period from 1977 to 2023, VPD increased significantly at a rate of 0.31 hPa per decade ($p < 0.05$), in parallel with a faster warming of T_{max} (0.30 °C per decade, $p < 0.05$) compared to T_{min} (0.27 °C per decade, $p < 0.05$). We further performed partial correlation analyses using annual land-average variables during each period. The partial correlation between T_{max} and VPD was 0.69 ($p < 0.05$) for 1950–1976 and 0.62 ($p < 0.05$) for 1977–2023, after controlling for T_{min} and SM. These correlations were stronger than those between T_{min} and

VPD during the same periods (-0.60 for 1950–1976 and -0.46 for 1977–2023, $p < 0.05$), controlling for T_{\max} and SM. Together, these findings reinforce the robustness of our conclusions, highlight the asymmetric effects of T_{\max} and T_{\min} on atmospheric dryness, and underscore the dominant role of T_{\max} in driving long-term changes in VPD.

Implications for drought and wildfire risk

Increased atmospheric dryness directly contributes to higher atmospheric evaporative demand, which has been identified in a recent study as playing an increasingly important role in the occurrence of severe droughts⁴⁶. To explore the relationship between atmospheric dryness and drought, we analyzed the correlation between annual VPD and the self-calibrated Palmer Drought Severity Index (scPDSI)⁵⁷ during 1980–2023. As a standardized drought index, lower values of scPDSI indicate more severe drought conditions. We found that VPD was significantly ($p < 0.05$) and negatively correlated with scPDSI across 47.7% of the global land area (Supplementary Fig. 22), suggesting a strong linkage between atmospheric dryness and drought conditions in these regions. These areas were mainly located in southwestern North America, eastern and southern South America, southern and eastern Europe, Central Asia, inland East Asia, and eastern Australia. Among the regions exhibiting significant negative VPD–scPDSI correlations, 68.6% experienced an increase in DTR and 69.3% experienced a decline in scPDSI. In contrast, among regions with either insignificant or positive VPD–scPDSI correlations, only 53.2% experienced increasing DTR. Furthermore, 62.9% of global land areas showed a significant negative correlation between DTR and scPDSI, with a spatial distribution pattern similar to that of regions with significant negative VPD–scPDSI correlations. These results indicate an important role of daytime warming in driving regional atmospheric drying and drought intensification⁵⁸. Recent increases in drought severity or frequency reported in regions such as the southwestern United States^{59,60}, Europe^{61,62}, inner East Asia^{63,64}, and South America^{65,66} may be closely linked to accelerated T_{\max} warming over recent decades (Fig. 1a).

Another major consequence of amplified atmospheric dryness is the increased frequency and severity of wildfires. Based on the fire weather index (FWI) from the European Centre for Medium-Range Weather Forecasts (ECMWF)⁶⁷, we found that a significant positive correlation exists between FWI and VPD (93.8% of land area) as well as between FWI and DTR (85.7% of land area) during 1980–2023 (Supplementary Fig. 23). These findings suggest a strong connection between faster daytime warming and heightened potential fire danger and intensity, as burned area is positively correlated with fire weather across much of the globe, including North and South America, Europe, and large parts of Asia⁶⁸. Recent wildfire events in the southwestern United States^{69,70}, Mediterranean Europe⁷¹, and South America⁷² are likely linked to increases in both DTR and VPD since the 1980s (Fig. 1a and Supplementary Fig. 3f).

Discussion

Our findings provide compelling evidence that stronger daytime warming over the past four decades has significantly contributed to increased atmospheric dryness. Given that the effects of SM on both T_{\max} and VPD are primarily mediated through evapotranspiration (ET), we conducted an additional ridge regression analysis by replacing SM with ET in Eqs. (3) and (5). Based on the ridge regression model defined as $VPD \sim f(T_{\max}, T_{\min}, ET)$, we found that T_{\max} has exerted a stronger positive influence on VPD than T_{\min} on the interannual scale. The spatial distribution of ridge regression coefficients (Supplementary Figs. 24a, 24b) is consistent with results from the original model defined in Eq. (3) (Fig. 1c, e), with spatial $r = 0.86$ and $r = 0.68$, respectively. Similarly, in the model defined as $AVP \sim f(T_{\max}, T_{\min}, ET)$, T_{\min} continued to show a more widespread and stronger positive effect on AVP compared to T_{\max} (Supplementary Fig. 25). The spatial distribution of regression

coefficients (Supplementary Figs. 25a, 25b) closely matches the corresponding results from the model based on Eq. (5) (Figs. 2c and 3d), with spatial $r = 0.84$ and $r = 0.86$, respectively. Previous studies suggest that ET is inherently difficult to measure accurately^{73,74}, particularly at large spatial scales⁷⁵, because it is influenced by a complex combination of environmental and biophysical factors⁷⁶. Therefore, we used SM as a more reliable proxy in the main analysis.

Additionally, the negative response of AVP to T_{\max} in water-limited areas of low- to mid-latitudes (Fig. 2c) can be disrupted by the sunlight-blocking effect of clouds. Days with higher AVP typically exhibit increased cloud cover⁷⁷, which reflects incoming solar radiation and lowers surface incident radiation, consequently decreasing T_{\max} . To mitigate this interference between AVP and T_{\max} due to radiation effects, we conducted an additional ridge regression analysis, derived from model defined as $AVP \sim f(T_{\max}, T_{\min}, SM, RS)$, where RS is surface incoming solar radiation, based on detrended and standardized variables from ERA5-Land from 1980 to 2023. The analysis reveals that the negative response of AVP to T_{\max} persisted across low- and mid-latitude regions (Supplementary Fig. 26a). The spatial distribution of the ridge regression coefficients closely aligns with the results from the analysis without including RS (Fig. 2c, spatial $r = 0.99$), indicating that the negative response of AVP to T_{\max} was not primarily caused by the sunlight-blocking effect of clouds. These analyses further confirm the robustness of our findings.

It is worth noting that SM increased significantly ($p < 0.05$) during 1950–1976 but showed a significant ($p < 0.05$) decline during 1977–2023 (Supplementary Fig. 27). This corresponds to the significant decreases in VPD and T_{\max} during the earlier period, and the significant increases in both variables in the later period. These contrasting trends raise another important question: since the 1980s, which effect has been dominant—the increase in T_{\max} leading to enhanced atmospheric dryness and then decreased SM, or the decline in SM reducing evaporative cooling and thereby contributing to higher T_{\max} and VPD? The recent increase in T_{\max} can be conceptually decomposed into two components. The first reflects the general warming trend shared with mean temperature and T_{\min} , which is widely attributed to increased greenhouse gas concentrations. The second represents an additional increase in T_{\max} relative to T_{\min} , primarily induced by radiation and mainly driven by widespread decreases in cloud cover and regional reductions in aerosol concentrations^{26,28,29}. SM plays a negligible role in the first component and only a limited role in the second²⁶. Therefore, SM decline is unlikely to be the main driver of the recent increases in T_{\max} . Regarding the reason of SM decline, given that land precipitation has shown little long-term change⁷⁸—suggesting relatively stable water input—the reduction in SM is more likely due to increased water loss from the soil, i.e., enhanced evaporation. Since increased VPD is a key driver of higher evaporative demand, this supports the interpretation that the dominant pathway is from increased T_{\max} leading to increased VPD and subsequently decreased SM, rather than the reverse.

The recent increase in VPD is clearly linked to global warming, and our findings reveal that this trend has been amplified by stronger daytime warming. Earth system models (ESMs) project a continued increase in VPD under future global warming scenarios^{8,9}. However, the projected magnitude of this increase may be underestimated if the continued rise in surface solar radiation (i.e., “global brightening”^{28,79,80}) and DTR, along with the amplification effect of sub-diurnal asymmetric warming identified in this study are not adequately accounted for. Moreover, the observed trend of increasing DTR since the 1980s has not been adequately captured in Coupled Model Inter-comparison Project Phase 6 (CMIP6) models²⁷. These findings underscore the urgent need to improve the simulation of future DTR trends and their influence on VPD, given that changes in atmospheric dryness could profoundly impact water cycling through land evapotranspiration¹¹, carbon cycling⁸¹, and increase the frequency and

intensity of extreme events such as drought and wildfires^{19,20}, underscoring the critical need for heightened attention.

Methods

Data

HadISD³⁷ is an in-situ sub-daily (reporting from 6-hourly to hourly) dataset based on the NOAA ISD dataset⁸². Multiple quality checks were applied to the dataset, including the removal of duplicates, detection of distribution gaps, and identification of climatological outliers^{37,83}. For station selection, we applied strict criteria: (1) valid days required minimum five paired observations of temperature and dew point temperature; (2) valid months allowed maximum 10 missing days and no more than 4 consecutive missing days²⁷; (3) stations from 1980–2023 were included only if missing months were below 2%. After the selection, 1398 stations were retained for analysis. Considering the lack of SM measurements in HadISD, we used SM from the ERA5-Land³⁸ reanalysis at the station sites.

The observations from flux towers of hourly temperature, VPD, and soil water content were obtained from FLUXNET2015⁴⁸. For SWC, we selected the shallowest measurement at a depth of 30 cm^{84,85}, representing the topsoil layer that directly interacts with the atmosphere. Only temperature, VPD, and SWC data with quality flags marked as “measured” or “good quality gapfill” were used. Time series encompassing complete observations over at least a three-year period were selected for analysis. After selection, 56 stations were retained for analysis, including 32 forest sites and 12 grassland sites. The forest sites included sites within deciduous broadleaf forests (DBF), evergreen needleleaf forests (ENF), evergreen broadleaf forests (EBF), and mixed forests (MF).

The hourly gridded temperature, dew point temperature, SM content of the soil layers and total evaporation were obtained from the ERA5-Land reanalysis dataset spanning 1950–2023 with a horizontal resolution of about 9 km. Here, SM content between 0 and 28 cm was calculated by summing up the moisture content for each layer weighted by the thickness of the layer¹². Monthly scPDSI data⁸⁶ were obtained from the Climatic Research Unit (CRU), covering global land areas from 1980 to 2023 at a spatial resolution of 0.5° × 0.5°. The scPDSI was calculated based on CRU TS 4.08 precipitation and temperature data, combined with fixed parameters related to local soil and surface characteristics. The index ranges from −4 (extremely dry) to +4 (extremely wet), representing water supply and demand as determined by a complex water-budget model that incorporates soil properties, historical precipitation, and potential evapotranspiration. FWI data were obtained from the Copernicus Emergency Management Service (CEMS)⁶⁷, derived from ECMWF ERA5 reanalysis-based historical simulations, covering 1980 to 2023 at a spatial resolution of about 0.25° × 0.25°. The FWI combines the Initial Spread Index and the Build-Up Index to provide a numerical rating of potential frontal fire intensity and is widely used to inform the public about fire danger conditions.

All gridded datasets were aggregated to a common 0.5° × 0.5° grid before analysis.

Calculation of vapor pressure deficit

VPD (hPa) was calculated using the following formula^{6,7}:

$$\text{VPD} = \text{SVP} - \text{AVP} \quad (7)$$

$$\text{SVP} = 6.1078 \times e^{\frac{a \times T_a}{a+b}} \quad (8)$$

$$\text{AVP} = 6.1078 \times e^{\frac{a \times T_{\text{dew}}}{a+b}} \quad (9)$$

Here, SVP is the saturated vapor pressure calculated based on the air temperature (T_a) in degrees Celsius. For T_a at or above 0 °C, a is

17.269 and b is 237.3. For T_a below 0 °C, a is 21.875 and b is 265.5⁶. AVP is the actual vapor pressure in hPa, which is defined as the vapor pressure of moist air at the ambient temperature or the saturation vapor pressure at the dew point^{7,41}. T_{dew} is the dew point temperature in degrees Celsius.

Ridge regression and attribution

Ridge regression³⁴ minimizes the effects of high multicollinearity (i.e., correlation) among the independent variables, particularly by alleviating interference caused by strong correlations between temperature/DTR and SM²⁶. The ridge regression was done separately using HadISD data at each station and ERA5-Land data at each grid box, with ERA5-Land SM data used in both analyses since HadISD does not include SM data. Prior to conducting the ridge regression analysis, long-term linear trends were removed from all variables. The detrended time series were then converted into z-scores by dividing the anomalies (from the linear trend) by their standard deviations for the period from 1980 to 2023. The ridge regression objective function (β) can be expressed as follows³⁴:

$$\beta^{\wedge} = \sum_{i=1}^n \left(y_i - \beta_0 - \sum \beta_j x_{ij} \right)^2 + \lambda \sum \beta_j^2 \quad (10)$$

where n is the number of total data points, y_i is the value of the dependent variable at time step i , β_0 is the intercept term, and β_j signifies the regression coefficient for the independent variable x_j whose value at i time step is x_{ij} . The optimal regularization parameter (λ) was determined using leave-one-out cross-validation (LOOCV). LOOCV is a special case of k -fold cross-validation where k (the number of subsamples) equals n (the number of observations). LOOCV is particularly appealing for small datasets, as it maximizes the size of the training set in each iteration. Here, for each value of λ , we performed LOOCV by iteratively excluding one observation, fitting the ridge model to the remaining data, and computing the squared prediction error for the excluded observation. This procedure was repeated for all observations, ensuring that each data point served once as the validation set. The LOOCV error for that λ was then calculated as the average of these squared errors. This procedure was repeated over a predefined set of λ values, and the λ with the lowest LOOCV error was selected as optimal. Formally, the LOOCV error for each λ was computed as:

$$\text{LOOCV error}(\lambda) = \frac{1}{n} \sum_{i=1}^n \left(y_i - y_{(i)}^{\lambda} \right)^2 \quad (11)$$

where $y_{(i)}^{\lambda}$ is the prediction for the i -th observation using the model trained without the i -th sample.

To quantify the statistical significance of the ridge regression coefficients, we applied a nonparametric bootstrap approach with 1000 iterations. In each iteration, the original dataset was resampled with replacement, and the ridge regression model was refitted using the LOOCV-optimized λ . This resulted in a distribution of regression coefficients for each predictor, from which the 95% confidence intervals (CIs) were derived using the 2.5th and 97.5th percentiles. A coefficient was deemed statistically significant if its CI did not include zero. This approach allows for robust inference without assuming normally distributed residuals and accounts for sampling variability.

The Durbin–Watson statistic⁸⁷ was used to detect the presence of autocorrelation at lag 1 in the residuals (prediction errors) from the regression analysis. If e_t denotes the residual at time t , the Durbin–Watson test statistic (d) is defined as

$$d = \frac{\sum_{t=2}^n (e_t - e_{t-1})^2}{\sum_{t=1}^n e_t^2} \quad (12)$$

where n is the number of time step. The value of d ranges from 0 to 4, with $d = 2$ indicating no autocorrelation. A value of $d < 2$ suggests positive autocorrelation, while $d > 2$ indicates negative autocorrelation. In our analysis, most Durbin–Watson statistics were close to 2, and there was no systematic deviation toward either positive or negative autocorrelation (Supplementary Figs. 4b, 5b and 9b), indicating little to no autocorrelation overall.

Random Forest regression analysis

We applied the RF algorithm to perform both interannual and trend analyses, based on the independent and dependent variables defined in Eqs. (2)–(6). Prior to conducting the interannual analysis, long-term linear trends were removed from all variables. The detrended time series were then converted into z-scores by dividing by the standard deviation of the anomalies. For the interannual analysis, the RF regression model was combined with the SHAP^{36,88} framework to quantify the relative importance of various environmental variables in driving the interannual variability of VPD, SVP, AVP, and RH. The SHAP method, grounded in the Shapley value concept from cooperative game theory, offers an enhanced approach over traditional local interpretable model-agnostic explanations by providing consistent and theoretically sound attributions of feature importance. For each response variable Y (e.g., VPD, SVP, etc.) and each sample i , the RF-predicted outcome can be decomposed as:

$$Y_i = Y_{\text{base}} + \sum_{j=1}^M \text{shap}(x_{ij}) \quad (13)$$

where Y_i is the RF prediction for sample i , Y_{base} is the mean prediction across all samples (i.e., the expected value of the model output), and $\text{shap}(x_{ij})$ is the SHAP value representing the contribution of predictor j to the prediction Y_i , and M is the number of predictor variables.

The relative importance of each predictor variable was quantified using the normalized magnitude of its absolute SHAP values across all samples. Specifically, for predictor j , the relative importance Rl_j was calculated as:

$$Rl_j = \frac{\frac{1}{N} \sum_{i=1}^N |\text{shap}(x_{ij})|}{\sum_{k=1}^M \frac{1}{N} \sum_{i=1}^N |\text{shap}(x_{ik})|} \quad (14)$$

where N is the total number of samples. The vertical bars denote absolute value. This metric captures the average absolute contribution of each variable to the model output, normalized across all predictors, and serves as a measure of overall variable importance. A predictor is considered the dominant driver if it shows the highest mean absolute SHAP value among all predictors, indicating that it contributes the most to the RF regression model output.

To determine whether each variable had a positive or negative influence on the response variable, we calculated the Theil–Sen slope between the values of each predictor and its corresponding SHAP values. A positive slope indicates that increases in the predictor tend to increase its SHAP value contribution (i.e., positive influence on Y), while a negative slope indicates that increases in the predictor tend to decrease its SHAP value contribution (i.e., negative influence on Y). This approach allows us to assess not only which variables are most important in driving model predictions, but also whether their effects are positive or negative.

For the trend analysis, we used all monthly data without detrending to train the RF model to predict VPD, SVP, and RH, as defined in Eqs. (2), (4), and (6), respectively. Model performance was evaluated using the out-of-bag (OOB) coefficient of determination (R^2) and mean squared error (MSE), which are internal cross-validation procedure inherent to RF and provide unbiased estimates of predictive accuracy without requiring a separate validation dataset. The long-

term impacts of sub-diurnal asymmetric warming on changes in VPD, SVP, and RH were then quantified using the RF model combined with a series of sensitivity experiments, as described below.

All RF models were trained individually at each station or grid point using 100 decision trees. Each tree independently predicted the response variable based on the provided predictors. To determine the optimal number of trees, we conducted a sensitivity analysis (Supplementary Fig. 28) using monthly variables from HadISD observations and the model defined in Eq. (2). The results show that the OOB MSE stabilizes once the number of trees exceeds 30, indicating that using 100 trees is sufficient for our purposes.

Sensitivity experiments for trend analysis

To assess the relative contribution of individual predictors (e.g., temperature and SM) to changes in a target variable (e.g., VPD or RH), we conducted a series of sensitivity experiments⁹ based on the RF regression models. Let Y denote the target variable (e.g., VPD or RH), and let $X = (X_1, X_2, \dots, X_n)$ represent the set of input predictors (e.g., T_{max} , T_{min} , SM). For each RF regression model, we first trained the model using the full dataset (1980–2023) to optimize its parameters, then applied the trained model on the input data to obtain fitted Y values (Y_{fitted}):

$$Y_{\text{fitted}} = f(X_1, X_2, \dots, X_n) \quad (15)$$

To quantify the contribution of a single predictor X_i to the change in Y , we performed sensitivity experiments by fixing X_i at its climatological monthly mean during a control period (1980–1982), while allowing all other variables to vary as observed. A new prediction $Y_{\sim X_i}$ was made under this perturbed condition:

$$Y_{\sim X_i} = f(X_1, \dots, X_{i,\text{ctrl}}, \dots, X_n) \quad (16)$$

where $X_{i,\text{ctrl}}$ is set to the multi-year mean of X_i for the corresponding calendar month calculated over the control period (1980–1982) and held constant throughout the time series. The contribution of X_i to the change in Y , denoted as Y_{X_i} , was then calculated as:

$$Y_{X_i} = Y_{\text{fitted}} - Y_{\sim X_i} \quad (17)$$

This process was repeated for each predictor, resulting in separate estimates of the contributions from each variable. This framework allowed us to isolate and quantify the role of each variable in driving long-term changes in the target variable.

Seasonal analysis and detrending for seasonality

In the analysis of FLUXNET site observations, seasons were defined as follows: March, April, May for spring (autumn), June, July, August for summer (winter), September, October, November for autumn (spring), and December, January, February for winter (summer) in the Northern Hemisphere (Southern Hemisphere).

To remove the seasonal cycle from the original daily data, we utilized a Fourier transform approach. First, we computed the mean daily values across all years and then applied a Fast Fourier Transform (FFT)⁵⁴ to these mean values. To retain only the primary seasonal components, we filtered the frequencies by zeroing out higher frequencies while preserving only the four lowest frequency components. We then performed an inverse FFT on the filtered data to reconstruct the seasonal component in the time domain. Finally, we subtracted the seasonal component from the original daily data to obtain the deseasonalized data. To maintain consistent 365-day years, we excluded the last day of the year during leap years.

Decoupling of SWC and DTR or VPD

Based on the daily observations at FLUXNET sites with seasonality removed, we calculated the SWC percentiles (4th through 96th, at 4-percentile intervals) at each tower site. These percentile values were then used to bin the data. Data for all variables (temperature, SWC, VPD, etc.) were sorted into 25 bins according to the percentiles of SWC. This binning procedure maintained the temporal match between data points. Only bins with more than 40 data points were included in the further analysis. Since SWC is largely decoupled from DTR and VPD within each SWC bin (Supplementary Fig. 15a), this method mitigates the influence of soil moisture on the impact of diurnal temperature variation on VPD.

Data availability

All data needed to evaluate the conclusions in the paper are present in the paper and/or the Supplementary Materials. The source data underlying Figs. 1–4 have been deposited in the Figshare repository and are available at <https://doi.org/10.6084/m9.figshare.29940365.v1>. The HadISD dataset is from <https://www.metoffice.gov.uk/hadobs/hadisd/>. The ERA5-Land dataset is from <https://cds.climate.copernicus.eu/datasets/reanalysis-era5-land?tab=download>. The FLUXNET2015 dataset is from <https://fluxnet.org/data/fluxnet2015-dataset/>. The scPDSI data is from <https://crudata.uea.ac.uk/cru/data/drought/#global>. The FWI data is from <https://ewds.climate.copernicus.eu/datasets/cems-fire-historical-v1>.

Code availability

The code for the analysis and mapping can be obtained from the Figshare repository (<https://doi.org/10.6084/m9.figshare.29940365.v1>).

References

- Wang, Y.-R., Hessen, D. O., Samset, B. H. & Stordal, F. Evaluating global and regional land warming trends in the past decades with both MODIS and ERA5-Land land surface temperature data. *Remote Sens. Environ.* **280**, 113181 (2022).
- Lee, H. et al. IPCC, 2023: *Climate Change 2023: Synthesis Report, Summary for Policymakers. Contribution of Working Groups I, II and III to the Sixth Assessment Report of the Intergovernmental Panel on Climate Change* (eds Core Writing Team, H. Lee and J. Romero). (IPCC, Geneva, Switzerland, 2023).
- WMO. *State of the global climate 2023*. (World Meteorological Organization, 2024).
- Perkins-Kirkpatrick, S. et al. Extreme terrestrial heat in 2023. *Nature Reviews Earth & Environment* **5**, 244–246 (2024).
- Cattiaux, J., Ribes, A. & Cariou, E. How Extreme Were Daily Global Temperatures in 2023 and Early 2024? *Geophys. Res. Lett.* **51**, e2024GL110531 (2024).
- Murray, F. W. On the Computation of Saturation Vapor Pressure. *Journal of Applied Meteorology and Climatology* **6**, 203–204 (1967).
- Buck, A. L. New Equations for Computing Vapor Pressure and Enhancement Factor. *Journal of Applied Meteorology and Climatology* **20**, 1527–1532 (1981).
- Ficklin, D. L. & Novick, K. A. Historic and projected changes in vapor pressure deficit suggest a continental-scale drying of the United States atmosphere. *J. Geophys. Res.:Atmos.* **122**, 2061–2079 (2017).
- Yuan, W., Zheng, Y., Piao, S., Ciais, P. & Yang, S. Increased atmospheric vapor pressure deficit reduces global vegetation growth. *Sci. Adv.* **5**, eaax1396 (2019).
- Fang, Z., Zhang, W., Brandt, M., Abdi, A. M. & Fensholt, R. Globally Increasing Atmospheric Aridity Over the 21st Century. *Earth's Future* **10**, e2022EF003019 (2022).
- Li, F. et al. Global water use efficiency saturation due to increased vapor pressure deficit. *Science* **381**, 672–677 (2023).
- Zhong, Z. et al. Disentangling the effects of vapor pressure deficit on northern terrestrial vegetation productivity. *Sci. Adv.* **9**, eadf3166 (2023).
- Roby, M. C., Scott, R. L. & Moore, D. J. P. High Vapor Pressure Deficit Decreases the Productivity and Water Use Efficiency of Rain-Induced Pulses in Semiarid Ecosystems. *J. Geophys. Res.:Biogeosci.* **125**, e2020JG005665 (2020).
- He, B. et al. Worldwide impacts of atmospheric vapor pressure deficit on the interannual variability of terrestrial carbon sinks. *Natl. Sci. Rev.* **9**, <https://doi.org/10.1093/nsr/nwab150> (2021).
- Hsiao, J., Swann, A. L. S. & Kim, S.-H. Maize yield under a changing climate: The hidden role of vapor pressure deficit. *Agricultural and Forest Meteorology* **279**, 107692 (2019).
- Lobell, D. B. et al. The critical role of extreme heat for maize production in the United States. *Nat. Clim. Change* **3**, 497–501 (2013).
- Xu, S. et al. Globally assessing the hysteresis between sub-diurnal actual evaporation and vapor pressure deficit at the ecosystem scale: Patterns and mechanisms. *Agricultural and Forest Meteorology* **323**, 109085 (2022).
- Li, S. et al. Increasing vapor pressure deficit accelerates land drying. *J. Hydrol.* **625**, 130062 (2023).
- Balch, J. K. et al. Warming weakens the night-time barrier to global fire. *Nature* **602**, 442–448 (2022).
- Luo, K., Wang, X., de Jong, M. & Flannigan, M. Drought triggers and sustains overnight fires in North America. *Nature* **627**, 321–327 (2024).
- Dai, A. Recent Climatology, Variability, and Trends in Global Surface Humidity. *J. Clim.* **19**, 3589–3606 (2006).
- Simmons, A. J., Willett, K. M., Jones, P. D., Thorne, P. W. & Dee, D. P. Low-frequency variations in surface atmospheric humidity, temperature, and precipitation: Inferences from reanalyses and monthly gridded observational data sets. *J. Geophys. Res.:Atmos.* **115**, <https://doi.org/10.1029/2009JD012442> (2010).
- Willett, K. M. et al. HadISDH land surface multi-variable humidity and temperature record for climate monitoring. *Clim. Past* **10**, 1983–2006 (2014).
- Vicente-Serrano, S. M. et al. Recent changes of relative humidity: regional connections with land and ocean processes. *Earth Syst. Dynam.* **9**, 915–937 (2018).
- Grossiord, C. et al. Plant responses to rising vapor pressure deficit. *New Phytol.* **226**, 1550–1566 (2020).
- Zhong, Z. et al. Reversed asymmetric warming of sub-diurnal temperature over land during recent decades. *Nat. Commun.* **14**, 7189 (2023).
- Huang, X. et al. Increasing Global Terrestrial Diurnal Temperature Range for 1980–2021. *Geophys. Res. Lett.* **50**, e2023GL103503 (2023).
- Wild, M. Global dimming and brightening: A review. *J. Geophys. Res.:Atmos.* **114** (2009).
- Zhou, L., Dickinson, R. E., Dai, A. & Dirmeyer, P. Detection and attribution of anthropogenic forcing to diurnal temperature range changes from 1950 to 1999: comparing multi-model simulations with observations. *Climate Dynamics* **35**, 1289–1307 (2010).
- Easterling, D. R. et al. Maximum and minimum temperature trends for the globe. *Science* **277**, 364–367 (1997).
- Vose, R. S., Easterling, D. R. & Gleason, B. Maximum and minimum temperature trends for the globe: An update through 2004. *Geophysical Research Letters* **32**, <https://doi.org/10.1029/2005GL024379> (2005).
- Phillips, C. L., Gregg, J. W. & Wilson, J. K. Reduced diurnal temperature range does not change warming impacts on ecosystem carbon balance of Mediterranean grassland mesocosms. *Global Change Biology* **17**, 3263–3273 (2011).

33. Intergovernmental Panel on Climate, C. *Climate Change 2013 – The Physical Science Basis: Working Group I Contribution to the Fifth Assessment Report of the Intergovernmental Panel on Climate Change*. (Cambridge University Press, 2014).
34. Hoerl, A. E. & Kennard, R. W. Ridge Regression: Biased Estimation for Nonorthogonal Problems. *Technometrics* **12**, 55–67 (1970).
35. Breiman, L. Random Forests. *Machine Learning* **45**, 5–32 (2001).
36. Lundberg, S. M. et al. From local explanations to global understanding with explainable AI for trees. *Nature Machine Intelligence* **2**, 56–67 (2020).
37. Dunn, R. J. H., Willett, K. M., Parker, D. E. & Mitchell, L. Expanding HadISD: quality-controlled, sub-daily station data from 1931. *Geosci. Instrum. Method. Data Syst.* **5**, 473–491 (2016).
38. Muñoz-Sabater, J. et al. ERA5-Land: a state-of-the-art global reanalysis dataset for land applications. *Earth Syst. Sci. Data* **13**, 4349–4383 (2021).
39. Dai, A. The diurnal cycle from observations and ERA5 in surface pressure, temperature, humidity, and winds. *Climate Dynamics* **61**, 2965–2990 (2023).
40. Dai, A. The diurnal cycle from observations and ERA5 in precipitation, clouds, boundary layer height, buoyancy, and surface fluxes. *Climate Dynamics* **62**, 5879–5908 (2024).
41. Allen, R. G. Crop evapotranspiration-Guidelines for computing crop water requirements-FAO Irrigation and drainage paper 56. (1998).
42. Li, Z., Yan, Z., Zhu, Y., Freychet, N. & Tett, S. Homogenized Daily Relative Humidity Series in China during 1960–2017. *Advances in Atmospheric Sciences* **37**, 318–327 (2020).
43. Willett, K. M. et al. HadISDH: an updateable land surface specific humidity product for climate monitoring. *Clim. Past* **9**, 657–677 (2013).
44. Dai, A., Trenberth, K. E. & Karl, T. R. Effects of Clouds, Soil Moisture, Precipitation, and Water Vapor on Diurnal Temperature Range. *J. Clim.* **12**, 2451–2473 (1999).
45. Paredes, P. & Pereira, L. S. Computing FAO56 reference grass evapotranspiration PM-ET_o from temperature with focus on solar radiation. *Agricultural Water Management* **215**, 86–102 (2019).
46. Penman, H. L. & Keen, B. A. Natural evaporation from open water, bare soil and grass. *Proceedings of the Royal Society of London. Series A. Mathematical and Physical Sciences* **193**, 120–145 (1948).
47. Massmann, A., Gentine, P. & Lin, C. When Does Vapor Pressure Deficit Drive or Reduce Evapotranspiration? *Journal of Advances in Modeling Earth Systems* **11**, 3305–3320 (2019).
48. Pastorello, G. et al. The FLUXNET2015 dataset and the ONEFlux processing pipeline for eddy covariance data. *Sci. Data* **7**, <https://doi.org/10.1038/s41597-020-0534-3> (2020).
49. Sulman, B. N. et al. High atmospheric demand for water can limit forest carbon uptake and transpiration as severely as dry soil. *Geophysical Research Letters* **43**, 9686–9695 (2016).
50. Novick, K. A. et al. The increasing importance of atmospheric demand for ecosystem water and carbon fluxes. *Nat. Clim. Change* **6**, 1023–1027 (2016).
51. Farquhar, G. D. Feedforward Responses of Stomata to Humidity. *Functional Plant Biology* **5**, 787–800 (1978).
52. Seneviratne, S. I. et al. Investigating soil moisture–climate interactions in a changing climate: A review. *Earth-Science Reviews* **99**, 125–161 (2010).
53. Zhou, S., Zhang, Y., Park Williams, A. & Gentine, P. Projected increases in intensity, frequency, and terrestrial carbon costs of compound drought and aridity events. *Science Advances* **5**, eaau5740 (2019).
54. Frigo, M. & Johnson, S. G. in *Proceedings of the IEEE International Conference on Acoustics, Speech and Signal Processing, ICASSP '98 (Cat. No.98CH36181)*, Vol. 1383, 1381–1384 (1998).
55. Liu, L. et al. Soil moisture dominates dryness stress on ecosystem production globally. *Nat. Commun.* **11**, 4892 (2020).
56. Gebrechorkos, S. H. et al. Warming accelerates global drought severity. *Nature* **642**, 628–635 (2025).
57. Wells, N., Goddard, S. & Hayes, M. J. A Self-Calibrating Palmer Drought Severity Index. *J. Clim.* **17**, 2335–2351 (2004).
58. Feng, Y., Sun, F. & Liu, F. SHAP-powered insights into short-term drought dynamics disturbed by diurnal temperature range across China. *Agricultural Water Management* **316**, 109579 (2025).
59. Wahl, E. R., Zorita, E., Diaz, H. F. & Hoell, A. Southwestern United States drought of the 21st century presages drier conditions into the future. *Communications Earth & Environment* **3**, 202 (2022).
60. Williams, A. P. et al. Large contribution from anthropogenic warming to an emerging North American megadrought. *Science* **368**, 314–318 (2020).
61. Markonis, Y. et al. The rise of compound warm-season droughts in Europe. *Sci. Adv.* **7**, eabb9668 (2021).
62. Büntgen, U. et al. Recent European drought extremes beyond Common Era background variability. *Nat. Geosci.* **14**, 190–196 (2021).
63. Zhang, P. et al. Abrupt shift to hotter and drier climate over inner East Asia beyond the tipping point. *Science* **370**, 1095 (2020).
64. Hessel, A. E. et al. Past and future drought in Mongolia. *Sci. Adv.* **4**, e1701832 (2018).
65. Lovino, M. A. et al. Agricultural flash droughts and their impact on crop yields in southeastern South America. *Environmental Research Letters* **20**, 054058 (2025).
66. Geirinhas, J. L. et al. Combined large-scale tropical and subtropical forcing on the severe 2019–2022 drought in South America. *npj Climate and Atmospheric Science* **6**, 185 (2023).
67. Vitolo, C. et al. ERA5-based global meteorological wildfire danger maps. *Sci. Data* **7**, 216 (2020).
68. Richardson, D. et al. Global increase in wildfire potential from compound fire weather and drought. *npj Climate and Atmospheric Science* **5**, 23 (2022).
69. Mueller, S. E. et al. Climate relationships with increasing wildfire in the southwestern US from 1984 to 2015. *Forest Ecology and Management* **460**, 117861 (2020).
70. Singleton, M. P., Thode, A. E., Sánchez Meador, A. J. & Iniguez, J. M. Increasing trends in high-severity fire in the southwestern USA from 1984 to 2015. *Forest Ecology and Management* **433**, 709–719 (2019).
71. Turco, M. et al. Exacerbated fires in Mediterranean Europe due to anthropogenic warming projected with non-stationary climate-fire models. *Nat. Commun.* **9**, 3821 (2018).
72. Úbeda, X. & Sarricolea, P. Wildfires in Chile: A review. *Global and Planetary Change* **146**, 152–161 (2016).
73. Li, Z., Chen, Y., Shen, Y., Liu, Y. & Zhang, S. Analysis of changing pan evaporation in the arid region of Northwest China. *Water Resources Research* **49**, 2205–2212 (2013).
74. Tran, B. N. et al. Uncertainty assessment of satellite remote-sensing-based evapotranspiration estimates: a systematic review of methods and gaps. *Hydrol. Earth Syst. Sci.* **27**, 4505–4528 (2023).
75. Zhang, K., Kimball, J. S. & Running, S. W. A review of remote sensing based actual evapotranspiration estimation. *WIREs Water* **3**, 834–853 (2016).
76. Xiong, Y., Chen, X., Tang, L. & Wang, H. Comparison of surface renewal and Bowen ratio derived evapotranspiration measurements in an arid vineyard. *J. Hydrol.* **613**, 128474 (2022).
77. Sherwood, S. C., Roca, R., Weckwerth, T. M. & Andronova, N. G. Tropospheric water vapor, convection, and climate. *Reviews of Geophysics* **48**, <https://doi.org/10.1029/2009RG000301> (2010).
78. Sheffield, J., Wood, E. F. & Roderick, M. L. Little change in global drought over the past 60 years. *Nature* **491**, 435–438 (2012).
79. Wild, M. Enlightening Global Dimming and Brightening. *Bull. Am. Meteorol. Soc.* **93**, 27–37 (2012).

80. Wild, M. et al. From Dimming to Brightening: Decadal Changes in Solar Radiation at Earth's Surface. *Science* **308**, 847–850 (2005).
81. Novick, K. A. et al. The impacts of rising vapour pressure deficit in natural and managed ecosystems. *Plant, Cell & Environment* n/a, <https://doi.org/10.1111/pce.14846> (2024).
82. Smith, A., Lott, N. & Vose, R. The Integrated Surface Database: Recent Developments and Partnerships. *Bull. Am. Meteorol. Soc.* **92**, 704–708 (2011).
83. Dunn, R. J. H. et al. HadISD: a quality-controlled global synoptic report database for selected variables at long-term stations from 1973–2011. *Clim. Past* **8**, 1649–1679 (2012).
84. Nie, C. et al. Effects of soil water content on forest ecosystem water use efficiency through changes in transpiration/evapotranspiration ratio. *Agricultural and Forest Meteorology* **308–309**, 108605 (2021).
85. Wang, L., Li, Y., Zhang, X., Chen, K. & Siddique, K. H. M. Soil water content and vapor pressure deficit affect ecosystem water use efficiency through different pathways. *J. Hydrol.* **640**, 131732 (2024).
86. Schrier, G. V. D., Barichivich, J., Briffa, K. R. & Jones, P. D. A scPDSI-based global data set of dry and wet spells for 1901–2009. *Journal of Geophysical Research Atmospheres* **118**, 4025–4048 (2013).
87. Durbin, J. & Watson, G. S. In *Breakthroughs in Statistics: Methodology and Distribution* (eds S. Kotz & N. L. Johnson) 237–259 (Springer New York, 1992).
88. Lundberg, S. M. & Lee, S.-I. In *Proceedings of the 31st International Conference on Neural Information Processing Systems* 4768–4777 (Curran Associates Inc., Long Beach, California, USA, 2017).

Acknowledgements

The study was supported by internal funding from Chalmers University of Technology. Z.Z. was supported by the VAPOR project (grant number 101154385), funded by the Horizon Europe, MSCA Postdoctoral Fellowships 2023. A.D. acknowledges the support of the National Science Foundation (grant number AGS-2015780).

Author contributions

Z.Z. designed the research, performed the analysis and wrote the draft; H.W.C., A.D., T.Z., B.H. and B.S. provided comments to improve the manuscript; H.W.C. supervised the project.

Funding

Open access funding provided by Chalmers University of Technology.

Competing interests

The authors declare no competing interests.

Additional information

Supplementary information The online version contains supplementary material available at <https://doi.org/10.1038/s41467-025-63672-z>.

Correspondence and requests for materials should be addressed to Hans W. Chen.

Peer review information *Nature Communications* thanks Shiqin Xu and the other, anonymous, reviewer for their contribution to the peer review of this work. A peer review file is available.

Reprints and permissions information is available at <http://www.nature.com/reprints>

Publisher's note Springer Nature remains neutral with regard to jurisdictional claims in published maps and institutional affiliations.

Open Access This article is licensed under a Creative Commons Attribution 4.0 International License, which permits use, sharing, adaptation, distribution and reproduction in any medium or format, as long as you give appropriate credit to the original author(s) and the source, provide a link to the Creative Commons licence, and indicate if changes were made. The images or other third party material in this article are included in the article's Creative Commons licence, unless indicated otherwise in a credit line to the material. If material is not included in the article's Creative Commons licence and your intended use is not permitted by statutory regulation or exceeds the permitted use, you will need to obtain permission directly from the copyright holder. To view a copy of this licence, visit <http://creativecommons.org/licenses/by/4.0/>.

© The Author(s) 2025